

Inversion Solutions of the Elliptic Cone Model for Disk Frontside Full Halo Coronal Mass Ejections

X. P. Zhao

W. W. Hansen Experimental Physics Laboratory, Stanford University, USA

¹ Short title: INVERSION SOLUTIONS OF ELLIPTIC CONE MODEL

2 **Abstract.** A new algorithm is developed for inverting 6 unknown elliptic cone
3 model parameters from 5 observed CME halo parameters. It is shown that the halo
4 parameter α includes the information on the CME propagation direction denoted by two
5 model parameters. Based on the given halo parameter α , two approaches are presented
6 to find out the CME propagation direction. The two-point approach uses two values of α
7 observed simultaneously by COR1 and COR2 onboard STEREO A and B. The one-point
8 approach combines the value of α with such simultaneous observation as the location of
9 CME-associated flare, which includes the information associated with CME propagation
10 direction. Model validation experiments show that the CME propagation direction
11 can be accurately determined using the two-point approach, and the other four model
12 parameters can also be well inverted, especially when the projection angle is greater than
13 60° . The propagation direction and other four model parameters obtained using the
14 one-point approach for six disk frontside full halo CMEs appear to be acceptable, though
15 the final conclusion on its validation should be made after STEREO data are available.

1. Introduction

Coronal mass ejections (CMEs) with an apparent (sky-plane) angular width of 360° are called full halo CMEs, and frontside full halo CMEs (FFH CMEs) if there are near-surface activities associated with the full halo CMEs. FFH CMEs with associated flares occurring within 45° and beyond 45° but within 90° from the solar disk center are called, respectively, disk and limb FFH CMEs (Gopalswamy et al., 2003). Disk FFH CMEs are mostly symmetric and ellipse-like. Limb FFH CMEs are, however, often asymmetric, including ragged structures as well as the smooth structure. The ragged structures are believed to be formed by the interaction between super-Alfvénic shocks and pre-existing coronal streamers and rays (Sheeley et al., 2000). This paper focus on the inversion solution of the elliptic cone model for disk FFH CMEs.

Disk FFH CMEs have been shown to be the most geoeffective kind of solar events. The geoeffectiveness rate of total disk FFH CMEs between 1997 and 2005 reaches 75% (Gopalswamy, Yashiro, and Akiyama, 2007), supporting the earlier result of 71% obtained using the disk FFH CMEs between 1997 and 2000 (Zhao and Webb, 2003). It is the higher end of the range of geoeffectiveness rate of solar activities. To predict when and in what percentage a disk FFH CME could generate intense geostorms, we need to determine when and which part of the huge interplanetary counterpart (ICME) of the disk FFH CME could hit earth's magnetosphere. It requires the knowledge of the size, shape, propagation direction and speed of ICMEs. However, coronagraphs record only the total content of free electrons in CMEs along the line of sight. A 2-D disk FFH CME cannot unambiguously provide any real geometrical and kinematic properties of a 3-D CME.

39 CMEs are believed to be driven by free magnetic energy stored in field-aligned
40 electric currents, and before eruption, the metastable structure with free magnetic energy
41 is confined by overlying arched field lines. The magnetic configuration of most, if not all,
42 CMEs is thus expected to be magnetic flux ropes with two ends anchored on the solar
43 surface (e.g. Riley et al., 2006), and the outer boundary of the top (or leading) part
44 of the ropes may be approximated by an ellipse with its major axis aligned with the
45 orientation of the ropes.

46 Most limb CMEs appear as planar looplike transients with a radially-pointed central
47 axis and a constant angular width. The existence of halo CMEs implies that the looplike
48 transients are three-dimensional. Both looplike and halolike CMEs show the evidence of
49 the rope-like magnetized plasma structure of CMEs. A conical shell (or cone) model,
50 i.e., a hollow body which narrows to a point from a round, flat base, was suggested to
51 qualitatively understand the formation of some full halo CMEs (Howard et al., 1982).

52 The cone model, as a proxy of the rope-like magnetized plasma structure of CMEs,
53 has been used to produce modeled elliptic halos, and the model parameters that are used
54 to produce the modeled halos can be determined by matching modeled halos to observed
55 halos (Zhao, Plunkett and Liu, 2002). The three model parameters of the circular cone
56 model can also be directly inverted from three halo parameters that characterize 2-D
57 elliptic halos (Xie et al., 2004).

58 The geometrical and kinematical properties obtained using the circular cone model
59 for the 12 May 1997 disk FFH CME (Zhao, Plunkett and Liu, 2002) were introduced
60 at the boundary of a 3-D MHD solar wind model (Odstrcil and Pizzo, 1999), and the
61 associated ICME near the earth's orbit were successfully reproduced (Odstrcil, Riley
62 and Zhao, 2004). It indicates that the idea for using cone-like geometric model to

63 invert model parameters from halo parameters is valid and useful in estimating the real
64 geometrical and kinematical properties for disk FFH CMEs.

65 It was found that the circular cone model can be used to reproduce only a limited
66 cases of halo CMEs, and that the elliptic cone model, i.e., a body which narrows
67 to an apex from an elliptic, flat base, would be better than the circular cone model
68 in approximating the rope-like CMEs (Zhao, 2005; Cremades and Bothmer, 2005).
69 However, the inversion solution of the elliptic cone model obtained using the approaches
70 of both Zhao (2005) and Cremades and Bothmer (2005) are often not unique.

71 In what follows we first define five halo parameters and three halo types for
72 disk FFH CMEs in Section 2. We then develop a new elliptic cone model with six
73 model parameters, and produce modeled halos that are expected to be observed by
74 multi-spacecraft, such as STEREO A, SOHO, and STEREO B in Section 3. The
75 inversion equation system of the elliptic cone model and the expressions of its solution are
76 established in Section 4. Based on two-point and one-point observations of CMEs, two
77 approaches are presented in Section 5 for determining the CME propagation direction
78 and other model parameters, and the model validation experiment is carried out to see
79 whether or not the established inversion equation system and the two approaches are
80 acceptable and useful. Finally we summarize and discuss the results in the last section.

81 **2. Description and classification of observed elliptic halos**

82 Figure 1 displays 6 disk FFH CMEs selected from Table 3 of Cremades (2005). The
83 onset date of the 6 events is shown on the top of each panel.

84 **2.1. Five halo parameters:** D_{se} , α , SA_{xh} , SA_{yh} , ψ

85 The white oval curve in each panel of Figure 1 is obtained by fitting to five selected
 86 points along the outer edge of each CME halo (see Cremades, 2005 for details). All white
 87 curves are ellipses and occur on the sky-plane $Y_h Z_h$ where Y_h and Z_h are the axes of the
 88 heliocentric ecliptic coordinate system, pointing to the west and north, respectively.

89 As shown in each panel, the short thick green line, D_{se} , denotes the distance between
 90 the solar disk center and the elliptic halo center, and axes X'_c and Y'_c are aligned with
 91 and perpendicular to D_{se} , respectively. The location of elliptic halos on the sky-plane
 92 can be specified using parameter D_{se} and the angle α between axes X'_c and Y_h . The
 93 shape and size of elliptic halos can be specified using two semi-axes of the halos, SA_{xh}
 94 and SA_{yh} , where SA_{xh} and SA_{yh} are located near the axes X'_c and Y'_c , respectively.
 95 The orientation of elliptic halos can thus be specified by the angle ψ between X'_c and
 96 SA_{xh} or Y'_c and SA_{yh} .

97 The five halo parameters, SA_{xh} , SA_{yh} , D_{se} , α and ψ , can be measured once the
 98 outer edge of halo CMEs is recognized. The top of each panel in Figure 1 shows the
 99 measured values of the 5 halo parameters for each event.

100 **2.2. Halo equations**

By using four halo parameters SA_{xh} , SA_{yh} , D_{se} , and ψ , a 2-D elliptic halo on the
 plane $X'_c Y'_c$ can be expressed

$$\begin{bmatrix} x'_c \\ y'_c \end{bmatrix} = \begin{bmatrix} D_{se} \\ 0 \end{bmatrix} + \begin{bmatrix} \cos \psi & \sin \psi \\ -\sin \psi & \cos \psi \end{bmatrix} \begin{bmatrix} x_{eh} \\ y_{eh} \end{bmatrix} \quad (1)$$

where

$$\begin{bmatrix} x_{eh} \\ y_{eh} \end{bmatrix} = \begin{bmatrix} SA_{xh} \sin \delta_h \\ SA_{yh} \cos \delta_h \end{bmatrix} \quad (2)$$

101 The symbol δ_h in equation (2) is the angle of radii of elliptic halos relative to SA_{yh} axis,
 102 and increases clockwise along an elliptic rim from 0° to 360° .

The halo observed in the sky-plane $Y_h Z_h$ can be obtained by rotating an angle of α as follows

$$\begin{bmatrix} y_h \\ z_h \end{bmatrix} = \begin{bmatrix} \cos \alpha & \sin \alpha \\ -\sin \alpha & \cos \alpha \end{bmatrix} \begin{bmatrix} x'_c \\ y'_c \end{bmatrix} \quad (3)$$

103 **2.3. Three types of observed halos**

104 It has been shown that the semi minor (major) axis of the elliptic halos formed by
 105 the circular cone model must be aligned with X'_c (Y'_c) axis. In other words, the halo
 106 parameter ψ must be equal to zero (See Xie et al., 2004 and Figure 2 of Zhao et al., 2002
 107 for details). Because of the uncertainty in identifying elliptic halos from coronagraph
 108 CME images, we consider SA_{xh} being nearly aligned with X'_c if $|\psi| < 10^\circ$.

109 Figure 1 shows that the halo parameter ψ that characterizes the orientation of
 110 elliptic halos can be any value between -45° and 45° . It means that the semi major (or
 111 minor) axis can be located anywhere on the plane of $X'_c Y'_c$. This fact suggests that most
 112 of disk FFH CMEs cannot be fitted or inverted using the circular cone model.

113 To distinguish the halos that may be inverted using the circular cone model from the
 114 halos that can be inverted using the elliptic cone model, we classify the observed elliptic
 115 halos into following three types,

$$TypeA : |\psi| < 10^\circ, SA_{xh} < SA_{yh};$$

$$TypeB : |\psi| < 10^\circ, SA_{xh} \geq SA_{yh};$$

$$TypeC : 10^\circ \leq |\psi| \leq 45^\circ.$$

116 The top left panel of Figure 1 shows a sample of Type A halo where SA_{xh} denotes
 117 the semi minor axis and is nearly aligned with X'_c axis. The Type A halo may be formed
 118 by the circular or the elliptic cone model. The top right panel shows a sample of Type B
 119 halo where SA_{xh} denotes the semi major axis though it is nearly aligned with X'_c . The
 120 four events shown in middle and bottom rows are Type C halos. Both Type B and Type
 121 C halos certainly cannot be produced using the circular cone model, and their model
 122 parameters must be inverted using the elliptic cone model.

123 Among 30 events in Table 3 of Cremades (2005), the number of Types A, B, and
 124 C is 3, 7 and 20, respectively. This distribution implies that only 10% of disk FFH
 125 CMEs may be reproduced and inverted using the circular cone model. Since Type A
 126 halos may also be formed by the elliptic cone model as shown in Sections 4 and 5, the
 127 model parameters inverted using the circular cone model for some Type A halos may
 128 significantly differ from the real ones.

129 **3. The elliptic cone model and model parameters**

130 Since the shape of 3-D rope-like CME plasma structure may be better approximated
 131 using the elliptic cone model, halos formed on the sky-plane by Thompson scattering
 132 along the line-of-sight may be better reproduced by projecting the elliptic cone base onto
 133 the sky-plane.

134 **3.1. Six elliptic cone model parameters: λ , ϕ , R_c , ω_y , ω_z , and χ**

135 As mentioned in Section 1, the elliptic cone model is a hollow body which narrows
 136 to its apex from an elliptic, flat base. The position of an elliptic cone base in the
 137 heliocentric ecliptic coordinate system, $X_h Y_h Z_h$, can be determined by locating the apex
 138 of the elliptic cone at the origin of the $X_h Y_h Z_h$ system, and by specifying the direction
 139 of the central axis of the elliptic cone in the $X_h Y_h Z_h$ with latitude λ and longitude ϕ .
 140 Here the X_h axis is aligned with the line-of-sight, pointing to the earth; λ and ϕ are
 141 measured with respect to the ecliptic plane $X_h Y_h$ and the line-of-sight X_h , respectively.

142 To define the size, shape and orientation of elliptic cone bases we introduce a ‘cone
 143 coordinate system’, $X_c Y_c Z_c$, and a ‘projection coordinate system’, $X'_c Y'_c Z'_c$ (see Figure 2
 144 for the definition of the three axes). As shown in Figure 2 and the left column of Figures
 145 3 and 4, the distance between the base and apex is denoted by R_c , and the half angular
 146 widths corresponding to two semi-axes of the cone bases, SA_{yb} and SA_{zb} , are by ω_y and
 147 ω_z . As shown in the bottom panel of the left column of Figures 3 and 4, the angle, χ ,
 148 between SA_{yb} and Y_c or between SA_{zb} and Z_c axes, specifies the orientation of the cone
 149 base. Therefore, six model parameters are needed to characterize the location, the shape
 150 and size, and the orientation of the base of a 3-D elliptic cone model in the $X_h Y_h Z_h$
 151 system.

152 **3.2. Relationship between λ , ϕ and β , α**

153 As shown in Figures 1 and 2, the projection angle β , i.e., the angle between the
 154 central axis X_c and its projection on the sky-plane, X'_c , denotes the latitude of the
 155 central axis relative to the sky-plane, and the observed halo parameter α the longitude
 156 of the central axis relative to westward Y_h .

The relationship between (β, α) and (λ, ϕ) is

$$\left\{ \begin{array}{l} \sin \lambda = \cos \beta \sin \alpha \\ \tan \phi = \cos \alpha / \tan \beta \end{array} \right\} \left\{ \begin{array}{l} \sin \beta = \cos \lambda \cos \phi \\ \tan \alpha = \tan \lambda / \sin \phi \end{array} \right\} \quad (4)$$

157 Equation (4) shows that parameter α (and β) depends on both λ and ϕ . Therefore, the
 158 observed halo parameter α provides information of both λ and ϕ . This information will
 159 be used in finding out the unknown parameter β , as shown in Section 5. It should be
 160 noted that positive angles are measured counterclockwise in rotation transformation.

161 In fact, the projection of the elliptic cone base onto the sky-plane depends only
 162 on the projection angle, β . We will replace λ and ϕ by β in establishing the inversion
 163 equation system of the elliptic cone model.

164 3.3. Projection of the elliptic cone base on the sky-plane

Given a set of values for the five model parameters $R_c, \omega_y, \omega_z, \chi, \beta$, a modeled halo
 on the plane $X'_c Y'_c$ can be obtained by the transformation of the rim of the elliptic cone
 base from coordinate system $X_e Y_e Z_e$ to $X_c Y_c Z_c$ and from $X_c Y_c Z_c$ to $X'_c Y'_c Z'_c$,

$$\begin{bmatrix} x'_c \\ y'_c \\ z'_c \end{bmatrix} = \begin{bmatrix} \cos \beta & \sin \beta \sin \chi & -\sin \beta \cos \chi \\ 0 & \cos \chi & \sin \chi \\ \sin \beta & -\cos \beta \sin \chi & \cos \beta \cos \chi \end{bmatrix} \begin{bmatrix} x_{eb} \\ y_{eb} \\ z_{eb} \end{bmatrix} \quad (5)$$

$$\begin{bmatrix} x_{eb} \\ y_{eb} \\ z_{eb} \end{bmatrix} = \begin{bmatrix} R_c \\ R_c \tan \omega_y \cos \delta_b \\ R_c \tan \omega_z \sin \delta_b \end{bmatrix} \quad (6)$$

165 where the symbol δ_b is the angle of radii of an elliptic base relative to SA_{yb} axis and
 166 increase along the rim of the elliptic base from 0° to 360° .

167 Using parameter α and equation (3), the modeled halo on the plane $Y_h Z_h$ can be
 168 obtained.

169 **3.4. Modeled halos**

170 Given a set of model parameters λ , ϕ , ω_y , ω_z , R_c and χ , as shown in the left column
 171 of Figures 3 or 4, we first calculate β and α using λ , ϕ and equation (4), then predict
 172 the elliptic halo on the sky-plane using equations (5),(6) and (3). The black ellipses in
 173 the right column of Figures 3 and 4 shows the modeled halos that are expected to be
 174 observed by coronagraphs onboard on three spacecraft, say STEREO A, SOHO, and
 175 STEREO B, simultaneously. As shown in each panel of right column in Figures 3 and
 176 4, the five halo parameters SA_{xh} , SA_{yh} , D_{se} , ψ , and α can be calculated based on the
 177 modeled halos.

178 The small green and big black dots in each panel denote, respectively, the semi axis
 179 of the modeled halos located near the Y'_c axis and the projection of the base semi-axis
 180 SA_{yb} on the $Y_h Z_h$ plane. Parameters ψ and χ' denote, respectively, the angular distance
 181 of the green and black dots from the Y'_c axis. The values of ψ and χ' in Figures 3 and 4
 182 depend on χ and β . The difference $\chi' - \chi$ and $\psi - \chi$ show the effect of the projection.
 183 Both χ' and ψ are zero when $\chi = 0$ (See Figure 3).

184 **4. Inversion equation system and its solution**

185 In order to invert the unknown model parameters from observed halo parameters,
 186 we first establish the inversion equation system that relates model parameters with halo
 187 parameters. We then find out the solution of the inversion equation system.

188 4.1. Inversion equation system of the elliptic cone model

189 The inversion equation system of the elliptic cone model may be established by
 190 comparing observed and modeled halos on the plane of $X'_c Y'_c$. Equations (1) and (2)
 191 describe observed elliptic halos on the plane of $X'_c Y'_c$ using four halo parameters SA_{xh} ,
 192 SA_{yh} , D_{se} , ψ . Equations (5) and (6) are the expressions of modeled elliptic halos on the
 193 same plane, but using five model parameters R_c , ω_y , ω_z , χ , and β .

194 By comparing the like items between equations (1) and (5), and setting $\delta_h = \delta_b + \Delta\delta$,
 195 the relationship between elliptic cone model parameters and elliptic CME halo parameters
 196 can be established

$$\begin{aligned}
 R_c \cos \beta &= D_{se} \\
 R_c \tan \omega_y \sin \beta \sin \chi &= SA_{xh} \cos \psi \sin \Delta\delta + SA_{yh} \sin \psi \cos \Delta\delta \\
 -R_c \tan \omega_z \sin \beta \cos \chi &= SA_{xh} \cos \psi \cos \Delta\delta - SA_{yh} \sin \psi \sin \Delta\delta \\
 R_c \tan \omega_y \cos \chi &= -SA_{xh} \sin \psi \sin \Delta\delta + SA_{yh} \cos \psi \cos \Delta\delta
 \end{aligned} \tag{7}$$

197 All model (halo) parameters occur in left (right) side of the equation system (7). By
 198 assuming $\Delta\delta = \delta_h - \delta_b \simeq \psi - \chi$, we have
 199

$$\begin{aligned}
 R_c \cos \beta &= D_{se} \\
 (R_c \tan \omega_y \sin \beta + a) \tan \chi &= b \\
 -R_c \tan \omega_z \sin \beta - b \tan \chi &= a \\
 R_c \tan \omega_y - b \tan \chi &= c
 \end{aligned} \tag{8}$$

200 where

$$\begin{aligned}
 a &= SA_{xh} \cos^2 \psi - SA_{yh} \sin^2 \psi \\
 b &= (SA_{xh} + SA_{yh}) \sin \psi \cos \psi \\
 c &= -SA_{xh} \sin^2 \psi + SA_{yh} \cos^2 \psi
 \end{aligned} \tag{9}$$

202

203 For Types A and B FFH CMEs, $\psi = 0$ and $\chi = 0$, equation systems (8), (9) become

$$\begin{aligned} R_c \cos \beta &= D_{se} \\ -R_c \tan \omega_z \sin \beta &= SA_{xh} \end{aligned} \quad (10)$$

$$204 \quad R_c \tan \omega_y = SA_{yh}$$

205 and when $\omega_y = \omega_z$, the number of model parameters equals the number of halo
206 parameters, equation system (10) reduce to the inversion equations for the circular cone
207 model (Xie et al., 2004).

208 It is interesting to note that $D_{se} = R_c \cos \beta$, showing that halo parameter D_{se}
209 depends on R_c and it increases as time increases. This time-dependent characteristic of
210 D_{se} is determined by the cone apex located at Sun's spherical center (see Figure 2 and
211 the left panels in Figures 3 and 4). There is a circular cone model that lays the apex of
212 the cone model at the solar surface, instead of the spherical center of the Sun assumed
213 here. For this kind of circular cone model, the parameter D_{se} , i.e., the distance between
214 the solar disk center and the elliptic halo center, is a constant (Michalek et al., 2003).
215 This different time variation of D_{se} may be used to determine which circular cone model
216 should be selected to invert the circular cone model parameters for a specific Type A
217 halo CME.

218 4.2. Solutions of the inversion equation system

219 From equation system (8), we have

$$\begin{aligned} R_c &= D_{se} / \cos \beta \\ \tan \omega_y &= \frac{-(a - c \sin \beta) + [(a + c \sin \beta)^2 + 4 \sin^2 \beta b^2]^{0.5}}{2R_c \sin \beta} \\ \tan \chi &= (R_c \tan \omega_y - c) / b \\ \tan \omega_z &= -(a + b \tan \chi) / R_c \sin \beta \end{aligned} \quad (11)$$

220

221 Equation system (11) shows that the four unknown model parameters in the left side
 222 can be calculated only when the model parameter β as well as the four halo parameters
 223 are given. For Types A and B when $\psi = 0$, equation system (11) becomes

$$\begin{aligned}
 R_c &= D_{se}/\cos\beta \\
 \tan\omega_y &= SA_{yh}/R_c \\
 \tan\omega_z &= -SA_{xh}/(R_c \sin\beta)
 \end{aligned}
 \tag{12}$$

224
 225 The solution of three model parameters R_c , ω_y and ω_z are determined by the model
 226 parameter β and three halo parameters D_{se} , SA_{xh} and SA_{yh} . Expressions (11) and
 227 (12) show that as β increases, R_c increases, and ω_y and ω_z decreases when the halo
 228 parameters are given. It should be noted that the half angular width ω_z inverted here
 229 corresponds to the angle measured clockwise from X_c to the lower side of the cone (see
 230 Figure 2). In what follows we show only the inverted value, neglecting its sign. When
 231 $\omega_y = \omega_z$, Equation system (12) becomes

$$\begin{aligned}
 \sin\beta &= SA_{xh}/SA_{yh} \\
 R_c &= D_{se}/\cos\beta \\
 \tan\omega &= SA_{yh}/R_c
 \end{aligned}
 \tag{13}$$

232
 233 In this case, three model parameters (ω , R_c , β) can be uniquely determined by three
 234 halo parameters (SA_{xh} , SA_{yh} , D_{se}). Expression (13) is just the inversion solution of the
 235 circular cone model derived by Xie et al. (2004).

236 **5. Determination of the propagation direction and inversion** 237 **solution for disk FFH CMEs**

238 As shown above, the number of unknown model parameters occurred in the solution
 239 expressions of the inversion equation system is always one more than the number of

240 given halo parameters. The only way to obtain the unique inversion solution of the
 241 elliptic cone model is to specify the model parameter β as well as halo parameters. We
 242 have pointed out in Section 3 that the given halo parameter α , that does not occur in
 243 the inversion equation system, contains the information of the model parameters ϕ and
 244 λ , and may be used to determine parameter β that depends on ϕ and λ .

245 The following two approaches can be used to determine the central axis direction
 246 (or the propagation direction) of disk FFH CMEs. Once the parameter β is calculated,
 247 the inversion solution of R_c , ω_y , ω_z and χ can be calculated using (11) for Type C and
 248 (12) for Types A and B.

249 5.1. Two-point observation

250 The parameter β can be determined by using two halo CME images observed at the
 251 same time by two spacecraft flying on the ecliptic plane. The three modeled halos in
 252 the right columns of Figures 3 or 4 are expected to be observed by STEREO A, SOHO,
 253 and STEREO B. Any two modeled CME halos provide two values of parameter α , say
 254 α_a and α_b , that contain information of two sets of λ and ϕ for the CME propagation
 255 direction. The corresponding two spacecraft are located at the ecliptic plane with their
 256 azimuthal difference of $\Delta\phi$. The central axis direction of a CME viewed from any two
 257 spacecraft are (λ, ϕ_a) and $(\lambda, \phi_a + \Delta\phi)$. Using equation system (4) we can easily
 258 calculate λ , ϕ_a and thus β . For instance, the two modeled halos in top right and middle
 259 right panels of Figure 3 show that $\alpha_a = -141.92^\circ$, $\alpha_b = -71.981^\circ$, and $\Delta\phi = 25^\circ$, we
 260 obtain $\phi_2 = -20.0^\circ$, $\lambda_2 = 15.00^\circ$ and $\beta_2 = 65.18^\circ$, as shown in the top right panel of
 261 Figure 3. They are exactly the same as the original values.

262 Using such calculated projection angle β and the values of four given halo parameters

263 D_{se} , SA_{xh} , SA_{yh} and ψ (see the top right panel of Figure 3), the model parameters R_c ,
 264 ω_y , ω_z and χ can be calculated using Equation systems (9) and (11). The parameters
 265 β_2 , λ_2 , ϕ_2 , r_{c2} , ω_{y2} , ω_{z2} , and χ_2 shown in the top right panel of Figure 3 denote the
 266 inverted results. The results shown in middle right and bottom right panels are obtained
 267 using the same method for the middle and bottom cases. All three model validation
 268 experiments show that Expressions (4) and (11) can be used to accurately invert the
 269 solution of elliptic cone model parameters for disk FFH CMEs with $\chi \simeq 0$. The red
 270 dashed ellipse is calculated using the inverted six model parameters. They completely
 271 agree with black ellipse.

272 All three black ellipses in Figure 3 are Type A, and produced by the same elliptic
 273 cone but with different ϕ . In practice, it is difficult, if not impossible, to determine if a
 274 Type A disk FFH CME is formed by a circular or a elliptic cone. To see the difference
 275 of inverted circular cone model parameters from the original ones, we first calculate
 276 the circular cone model parameters using (13) and three halo parameters (D_{se} , SA_{xh} ,
 277 SA_{yh}), and then produce the green dotted ellipses on the basis of the inverted model
 278 parameters. Although the green ellipses are also completely agree with the black ellipses,
 279 the obtained values for three circular cone model parameters are totally different from
 280 the original elliptic cone model parameters (see left column of Figure 3). For instance,
 281 the inverted circular cone model parameters for the top right panel are $R_c = 2.69$,
 282 $\omega_y = \omega_z = 57.36$, $\beta = 38.65$, and $\lambda = 28.79^\circ$, and $\phi = -44.55^\circ$. They are certainly not
 283 usable. This experiment shows that even for Type A disk FFH CMEs, it is not safe to
 284 use the circular cone model to invert the model parameter.

285 Figure 4 is the same as Figure 3, but the values of ω_y , ω_z and χ are different from
 286 Figure 3 (see the left column). The red dashed ellipses in the right column of Figure 4

287 are obtained using the same way as Figure 3 but their agreement with black ellipses is
 288 worse than Figure 3. Comparison of the inverted model parameters with the original
 289 ones show that the parameters λ , ϕ , R_c and ω_y agree with original ones very well; and
 290 dependent on β , the inverted ω_z is slightly different from original and the inverted χ
 291 may be significantly different from original.

292 5.2. One-point observation

293 A CME can propagate in any direction (ϕ, λ) in the 3-D space. For a specified value
 294 of α , all possible sets of ϕ and λ are reduced from whole ϕ - λ plane to a specific curve, as
 295 shown in each panel of Figure 5. The six curves in Figure 5 correspond to the six values
 296 of α shown in Figure 1. These curves are obtained by assuming that the possible value
 297 of β for disk FFH CMEs ranges from 45° to 90° .

298 To search for the optimum central axis direction (β or ϕ_{ce} , λ_{ce}) among all possible
 299 directions on a curve corresponding to a specific value of the halo parameter α , it is
 300 necessary to use additional information that is associated with the CME propagation
 301 direction or the center of CME source region.

302 CME-associated flares or active regions are believed to be located near the center of
 303 CME source region (e.g., Zhao and Webb, 2003), though they are often located near one
 304 leg of CMEs (e.g., Plunkett et al., 2001). The dot in each panel of Figure 5 denotes the
 305 location of the CME-associated flare.

306 Taking consideration the effect of interaction between higher-latitude high speed
 307 streams and lower-latitude CME in the declining and minimum phases of solar activity,
 308 it was suggested that the optimum propagation direction may be found by moving the
 309 flare location southwardly, i.e., by lowering the flare latitude while keeping the flare

310 longitude constant (Cremade, 2005). This approach cannot work for all cases shown in
 311 Figure 5, especially for the cases of top-left and bottom-left panels. In addition, this
 312 approach may not be working for all phases of solar activity.

313 We find out the optimum central axis direction among all possible direction on a
 314 curve by finding out the minimum distance between the dot and the curve in each panel
 315 of Figure5. The calculated β and $(\phi_{ce}, \lambda_{ce})$ are shown in the south-west quadrant of each
 316 panel.

317 It should be noted that the location of flares is often specified using the latitude
 318 and longitude measured in the heliographic coordinate system, i.e., the latitude and
 319 longitude measured with respect to the solar equator, instead of the solar ecliptic plane.
 320 The effect of B0 angle (the heliographic latitude of the Earth) should be corrected before
 321 finding out the optimum model parameter β . The symbols ϕ_{fs}, λ_{fs} and ϕ_{fe}, λ_{fe} denote
 322 longitude and latitude of CME-associated flares measured in the heliographic and the
 323 heliocentric ecliptic coordinate systems, respectively. We first calculate ϕ_{fe}, λ_{fe} using
 324 ϕ_{fs}, λ_{fs} , and $B0$, then find out ϕ_{ce}, λ_{ce} using ϕ_{fe}, λ_{fe} (the dot) and α (the curve).

325 Once the optimum value of the projection angle β is obtained, the model parameters
 326 that are supposed to form the observed halos (white ellipses in Figures 6, 7, and 8) can
 327 be inverted using observed four halo parameters SA_{xh}, SA_{yh}, D_{se} , and ψ , as shown on
 328 the top of each panel in Figure 1. Figures 6, 7, and 8 display the calculated elliptic
 329 cone model parameters for the six disk FFH CMEs in Figure 1. The green ellipse in
 330 each panel of Figures 6, 7 and 8 is calculated from the inverted six model parameters
 331 and equation system (5), (6) and (3). The comparison of the green ellipses with the
 332 white ellipses show that the agreement between green and white ellipses depend on the
 333 parameters β and χ . When $\chi < 30^\circ$ the agreement is reasonable, as shown in Figures 6

334 and 7. When inverted $\chi > 30^\circ$ the difference increases as β decreases as shown in Figure
 335 8. It is similar to what we find out from Figure 4. The similarity might suggest that the
 336 projection angle β obtained using one-point approach is acceptable.

337 FFH CMEs of Types B and C can be fitted only by the elliptic cone model. Type
 338 A event, such as the 9 October 2001 event in the top panel of Figure 6, can be formed
 339 by projecting a circular or elliptic base onto the sky-plane, and thus can be fitted by the
 340 elliptic or circular cone model. As shown by Equations (12) and (13) when $\omega_y = \omega_z$, the
 341 inversion solutions obtained using circular and elliptic cone models should be the same if
 342 the real base is a circular one.

343 To compare the inversion solutions of the elliptic cone model with that of the
 344 circular cone models, we fit the Type A halo of the 9 October 2001 using the circular
 345 cone model as well as the elliptic cone model. Listed in the panel are the inverted circular
 346 cone model parameters as well as the inverted elliptic cone model parameters. The
 347 black dashed ellipse is obtained using the circular cone model parameters. Although the
 348 agreement of both the green and black ellipses with the observed white ellipse is equally
 349 well, the elliptic cone model parameters are significantly different from the circular cone
 350 model parameters. The central axial direction inverted from the circular cone model (the
 351 open circle in the top left panel of Figure 5) is located far from the the CME-associated
 352 flare location (the black dot), and the distance from the solar center to the elliptic base,
 353 $R_c = 18.4$ solar radii, appears to be too far from the solar surface to produce observed
 354 brightness of the halo CME. Therefore the Type A halo of the 9 October 2001 event is
 355 caused by the elliptic cone model, instead of the circular cone model.

356 6. Summary and discussions

357 We have shown that on the sky-plane $Y_h Z_h$, disk FFH CMEs provide 5 halo
 358 parameters, and can be classified into Types A, B, and C, depending on the major axis
 359 of elliptic halos being perpendicular to, aligned with, or anywhere else from the direction
 360 from the solar disk center to the CME halo center.

361 The elliptic cone model needs 6 model parameters to characterize its morphology in
 362 the heliocentric ecliptic coordinate system $X_h Y_h Z_h$.

363 However, the morphology of the CME halo and the elliptic cone base in the
 364 projection coordinate system $X'_c Y'_c Z'_c$ can be described by 4 halo and 5 model
 365 parameters, respectively. In the system $X'_c Y'_c Z'_c$, the halo parameter α disappears, and
 366 the two model parameters λ and ϕ that denote the CME propagation direction in
 367 $X_h Y_h Z_h$ are replaced by one new model parameter β , the projection angle.

368 On the other hand, the axis Y'_c is the reference axis for measuring the orientation
 369 of both elliptic CME halos and elliptic cone bases. The inversion equation system of the
 370 elliptic cone model and its solution can thus be established by setting $\delta_h = \delta_b + \Delta\delta$, and
 371 assuming $\Delta\delta = \delta_h - \delta_b \simeq \psi - \chi$, and by comparing the like term in the expressions
 372 between modeled and observed halos in the $X'_c Y'_c Z'_c$ system.

373 The halo parameter α that does not occur in the inversion equation system depends
 374 on both latitude and longitude of the CME propagation direction (λ, ϕ) , and has
 375 been used to estimate the model parameter β on the basis of two-point or one-point
 376 observations of halo CMEs.

377 The two-point approach uses two values of α observed at the same time by COR1
 378 and COR2 onboard STEREO A and B. Model validation experiments have been carried

379 out for the cases of $\chi = 0^\circ$ and $\chi = -30^\circ$. The experiment results show that the CME
 380 propagation direction can be accurately determined by the two-point approach. The
 381 other four model parameters can also be accurately inverted for the case of $\chi = 0^\circ$, i.e.
 382 for Types A and B disk FFH CMEs. For the case of $\chi = -30^\circ$, i.e., Type C disk FFH
 383 CMEs, the obvious difference occurs only between inverted and original parameter χ ,
 384 the orientation of the elliptic cone base. These results imply that the difference is caused
 385 by the assumption of $\Delta\delta = \delta_h - \delta_b \simeq \psi - \chi$, that is made in establishing the inversion
 386 equation system (8).

387 The one-point approach combines the value of α with such simultaneous observation
 388 as the location of CME-associated flare, which includes the information associated with
 389 CME propagation direction. The six events displayed in Figure 1 for showing the three
 390 types of disk FFH CMEs have been tested. Both the propagation direction obtained
 391 using one-point approach and the other four model parameters inverted appear to be
 392 reasonable and acceptable. The agreement between the observed halos and modeled
 393 halos depends mainly on the projection angle β . It is the same as what we find in
 394 the model validation experiments for the two-point approach. The STEREO data are
 395 expected to be used to finally determine in what extent the CME propagation direction
 396 obtained from the one-point approach is correct.

397 After obtaining the elliptic cone model parameters, the CME propagation speed can
 398 be determined using the method similar to Zhao et al (2002) or Xie et al (2004).

399 The inversion equation system of the elliptic cone model and the expression of its
 400 solution can be reduced to that of the circular cone model. For Type A modeled halos in
 401 Figure 3 and observed halos in Figure 6, three circular cone model parameters are also
 402 inverted on the bases of three halo parameters. Both results show significant differences

403 from the inverted elliptic cone model parameters, though the modeled halos calculated
404 using the circular cone model parameters completely agree with the observed halos.

405 It is difficult, if not impossible, to distinguish halos produced by elliptic cone from
406 that by circular cone. The circular cone model should be used with utmost care lest it
407 leads to erroneous conclusions. The inverted elliptic cone model parameters should be
408 the same as the inverted circular cone model parameters if the base of the cone-like CME
409 structure is circular. It is suggested to use the elliptic cone model to invert the geometric
410 and kinematic properties for all Type A disk FFH CMEs.

411 There are some disk FFH CMEs that are not purely elliptic. Some of them may
412 be formed by ice-cream cone models. It has been shown that by determining the halo
413 parameters from the rear part of the asymmetric halos, the elliptic cone model presented
414 here can still be used to invert the model parameters for these asymmetric disk FFH
415 CMEs (X. P. Zhao, Ice cream cone models for halo coronal mass ejections, in preparation,
416 2007).

417 The accuracy of inversion solutions depends significantly on the halo parameters
418 measured from observed disk FFH CMEs. We have developed codes to calculate the five
419 halo parameters on the basis of the outer edge of halo CMEs. All the white elliptic outer
420 edge shown in Figure 1 were determined using the 5-point technique (see Cremades,
421 2005, for details). To further improve the accuracy of the halo parameters we plan to
422 automatically and more objectively recognize the outer edge of disk FFH CMEs using
423 the pattern or feature recognition technique.

424 **7. acknowledgments**

425 We thank Dr. H. Cremades for sending us her Ph. D. Thesis and her data product
426 for 30 disk FFH CMEs. The six images in Figures 1 are selected from the 30 disk FFH
427 CMEs. This work is supported by NASA grants NAGW 2502 and NAG5-3077, by NSF
428 grant ATM9400298.

429 **References**

- 430 Cremades, H., Three-dimensional configuration and evolution of coronal mass ejections,
431 Ph. D. thesis, Copernicus GmbH, Katlenburg-Lindau, Germany, ISBN:
432 3-936586-40-3, 2005.
- 433 Cremades, H. and V. Bothmer, Geometrical properties of coronal mass ejections, in *Proc.*
434 *IAL symp. 226 on Coronal and Stellar Mass Ejections*, eds. K. P. Dere, J. Wang,
435 and Y. Yan, 48, 2005.
- 436 Gopalswamy, N., A. Lara, S. Yashiro, S. Nunes, and R. A. Howard, Coronal mass
437 ejection activity during solar cycle 23, in *Proc. ISCS 2003 Symposium on Solar*
438 *Variability as an Input to Earth's Environment*, ESA-SP 535, p. 403, 2003.
- 439 Gopalswamy, N., S. Yashiro, and S. Akiyama, Geoeffectiveness of halo coronal mass
440 ejections, *Journal Geophys. Res.*, *in press*,, 2007.
- 441 Howard, R. A., D. J. Michels, N. R. Sheeley Jr., and M. J. Koomen, The observation of
442 a coronal transient directed at earth, *Astrophys. J.*, *263*, 1101, 1982.
- 443 Michalek, G., N. Gopalswamy and S. Yashiro, A new method for estimating widths,
444 velocities, and source location of halo coronal mass ejections, *Astrophys. J.*, *584*,
445 472-478, 2003.
- 446 Plunkett, S. P., et al., Solar source regions of coronal mass ejections and their geomagnetic
447 effects, *J. Atmos. Sol. Terr. Phys.*, *63*, 389, 2001.
- 448 Odstrcil, D., P. Riley, and X. P. Zhao, Numerical simulation of the 12 may 1997
449 interplanetary cme event, *Journal Geophys. Res.*, *109*, a02116, 2004.
- 450 Riley, P., C. Schatzman, H. V. Cane, I. G. Richardson, N. Gopalswamy, On the rates of
451 coronal mass ejections: remote solar and in situ observations, *Astrophys. J.*, *647*,

- 452 648, 2006.
- 453 Sheeley, N. R. jr., W. N. Hakala, and Y.-M. Wang, Detection of coronal mass ejection
 454 associated shock waves in the outer corona, *Journal Geophys. Res.*, *105*, 18169,
 455 2000.
- 456 Xie, H., L. Ofman and G. Lawrence, Cone model for halo cmes: applica-
 457 tion to space weather forecasting, *Journal Geophys. Res.*, *109*, A03109,
 458 doi:10.1029/2003ja010226, 2004.
- 459 Zhao, X. P., Determination of geometrical and kinematical properties of frontside halo
 460 coronal mass ejections, in *Proc. IAL symp. 226 on Coronal and Stellar Mass*
 461 *Ejections*, eds. K. P. Dere, J. Wang, and Y. Yan, 42, 2005.
- 462 Zhao, X. P., Ice cream cone models for halo coronal mass ejections, in preparation, 2007.
- 463 Zhao, X. P., S. P. Plunkett and W. Liu, Determination of geophysical and kinematical
 464 properties of halo coronal mass ejections using the cone model, *Journal Geophys.*
 465 *Res.*, *107*, No A8, doi:10.1029/2001JA009143, 2002
- 466 Zhao, X. P. and D. F. Webb, Source regions and storm effectiveness of frontside
 467 full halo coronal mass ejections, *Journal Geophys. Res.*, *108*, 1234,
 468 doi:10.1029/2002JA009606, 2003.

469 X. P. Zhao, W. W. Hansen Experimental Physics Laboratory, Stanford University,
 470 Stanford, CA 94305-4085. (e-mail:xuepu@sun.stanford.edu)

471 Received _____

472 This manuscript was prepared with AGU's L^AT_EX macros v5, with the extension
 473 package 'AGU++' by P. W. Daly, version 1.6b from 1999/08/19.

Figure 1.

Figure 2.

Figure 3.

Figure 4.

474 Figure Captions

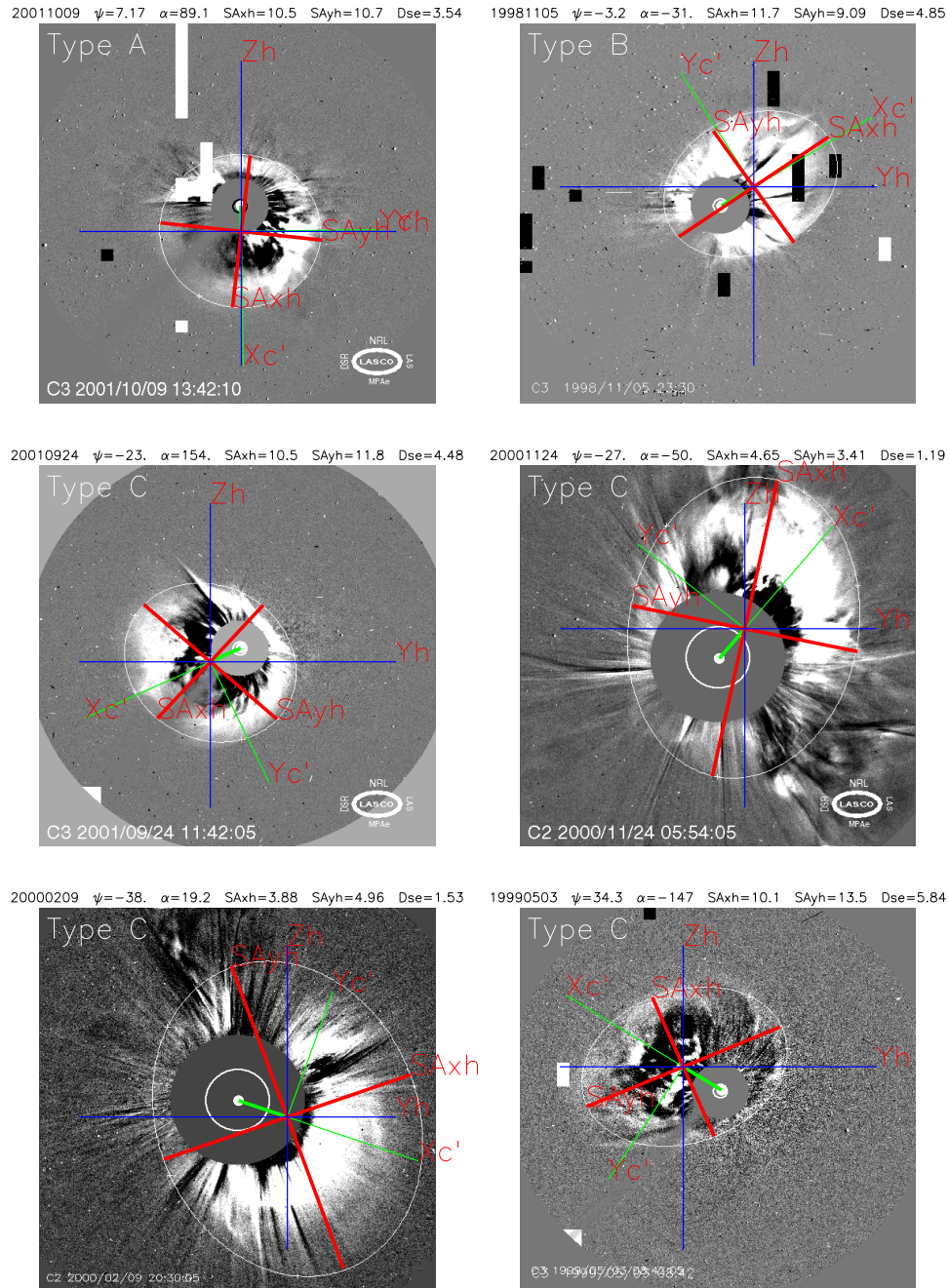


Figure 1. Definition of 5 halo parameters (SA_{xh} , SA_{yh} , ψ , D_{se} , α) and Types A, B, C for disk frontside full halo CMEs (see text for details). Here X'_c and Y'_c are, respectively, aligned with and perpendicular to the direction from the solar disk center to the halo center, D_{se} (the short thick green line). Parameters ψ and α denote the angles between SA_{yh} and Y'_c and between X'_c and Y_h , respectively.

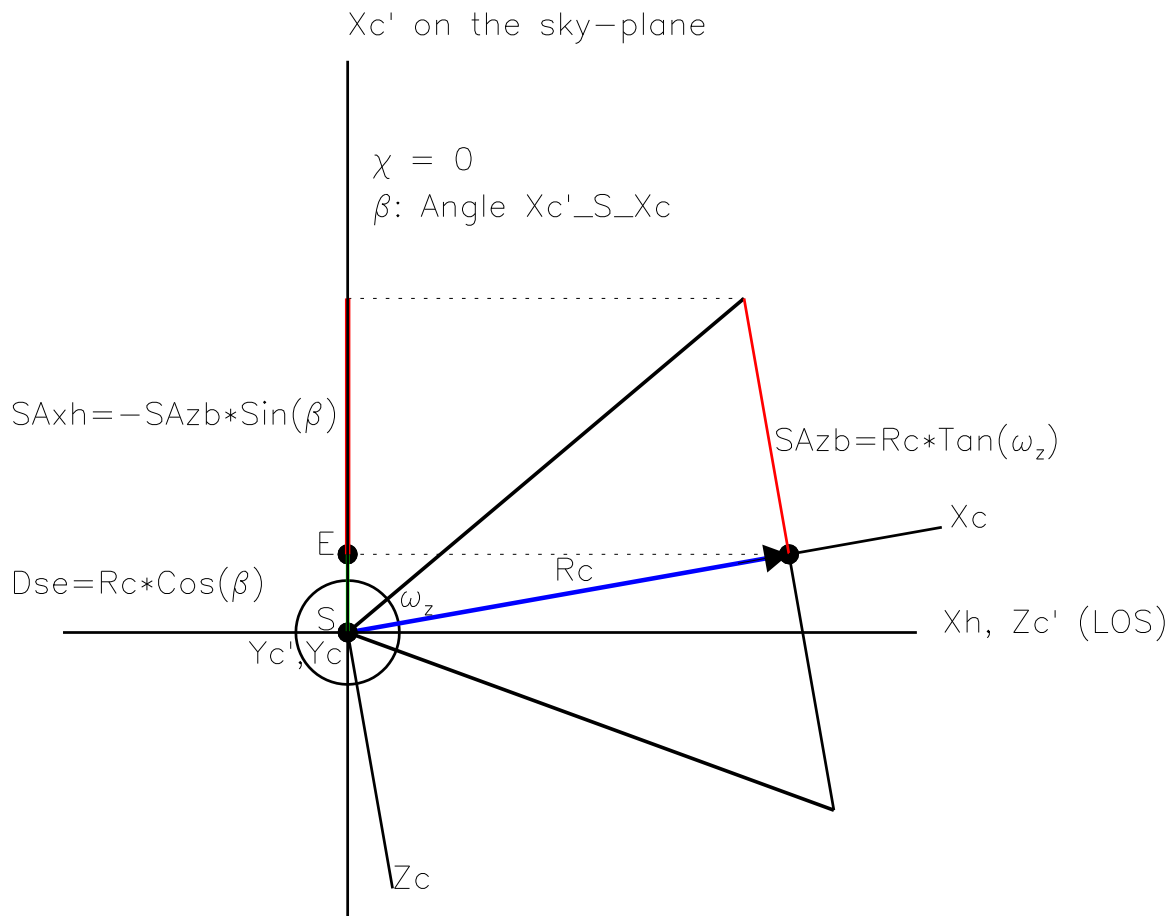


Figure 2. Three coordinate systems used in the transformation from the cone coordinate system $X_c Y_c Z_c$ through the projection coordinate system $X'_c Y'_c Z'_c$ to the heliocentric ecliptic coordinate system $X_h Y_h Z_h$. The projection of the elliptic cone base onto the sky-plane takes place from $X_c Y_c Z_c$ to $X'_c Y'_c Z'_c$, and depends only on the parameter β , the angle from X_c to X'_c . The circle with a radius of 2 denotes the occulting disk of Coronagraph C2 onboard SOHO.

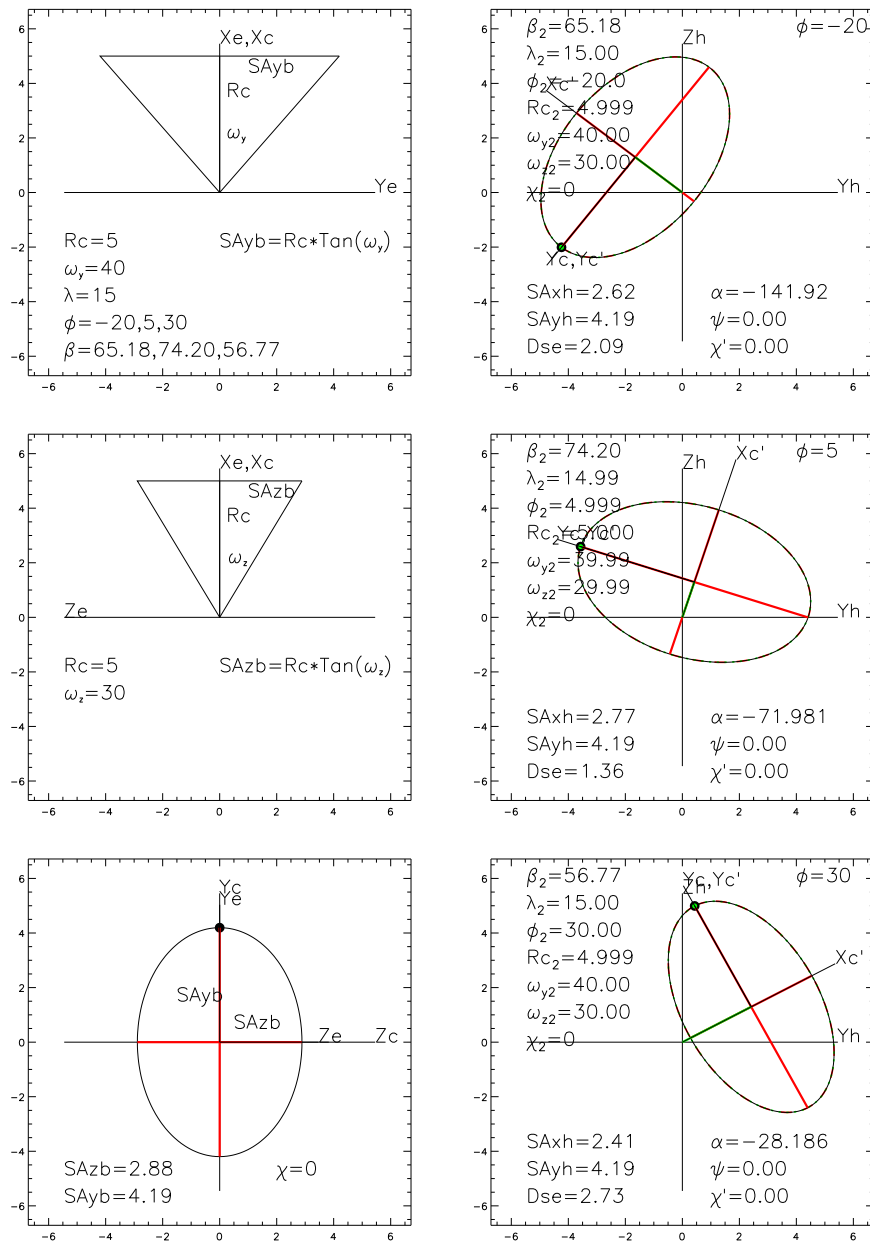


Figure 3. The left column shows the definition of elliptic cone model parameters R_c , ω_y , ω_z , and χ , and a set of values for 6 elliptic cone model parameters. The right column shows the three modeled halos (black ellipses) that are supposed to be observed by three spacecraft located on the ecliptic plane with different azimuths. The inverted model parameters with subscript '2' are also shown in each panel in the right column. The green and red dashed ellipses are modeled halos calculated using inverted elliptic and circular cone model parameters, respectively.

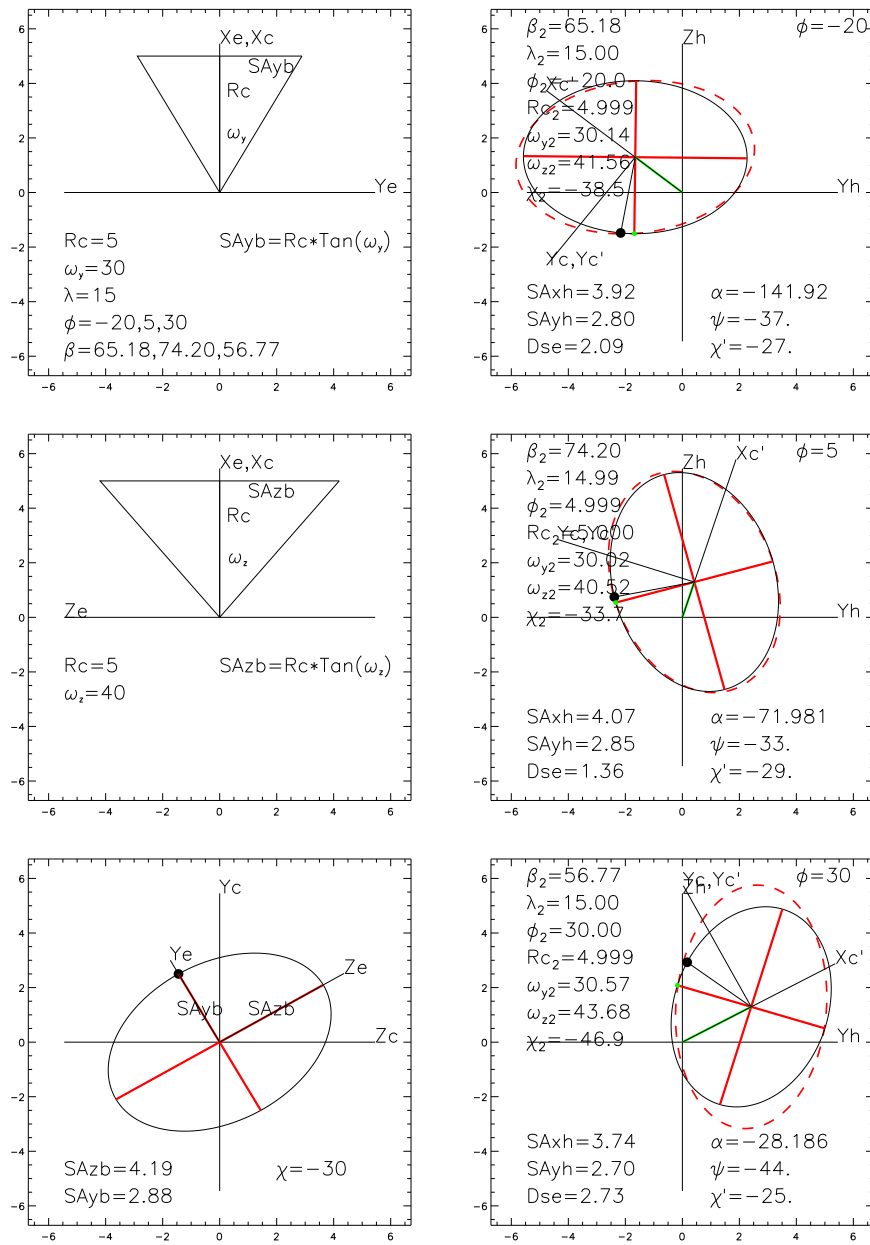


Figure 4. The same as Figure 3 but with different ω_y , ω_z , and χ , as shown in the left column.

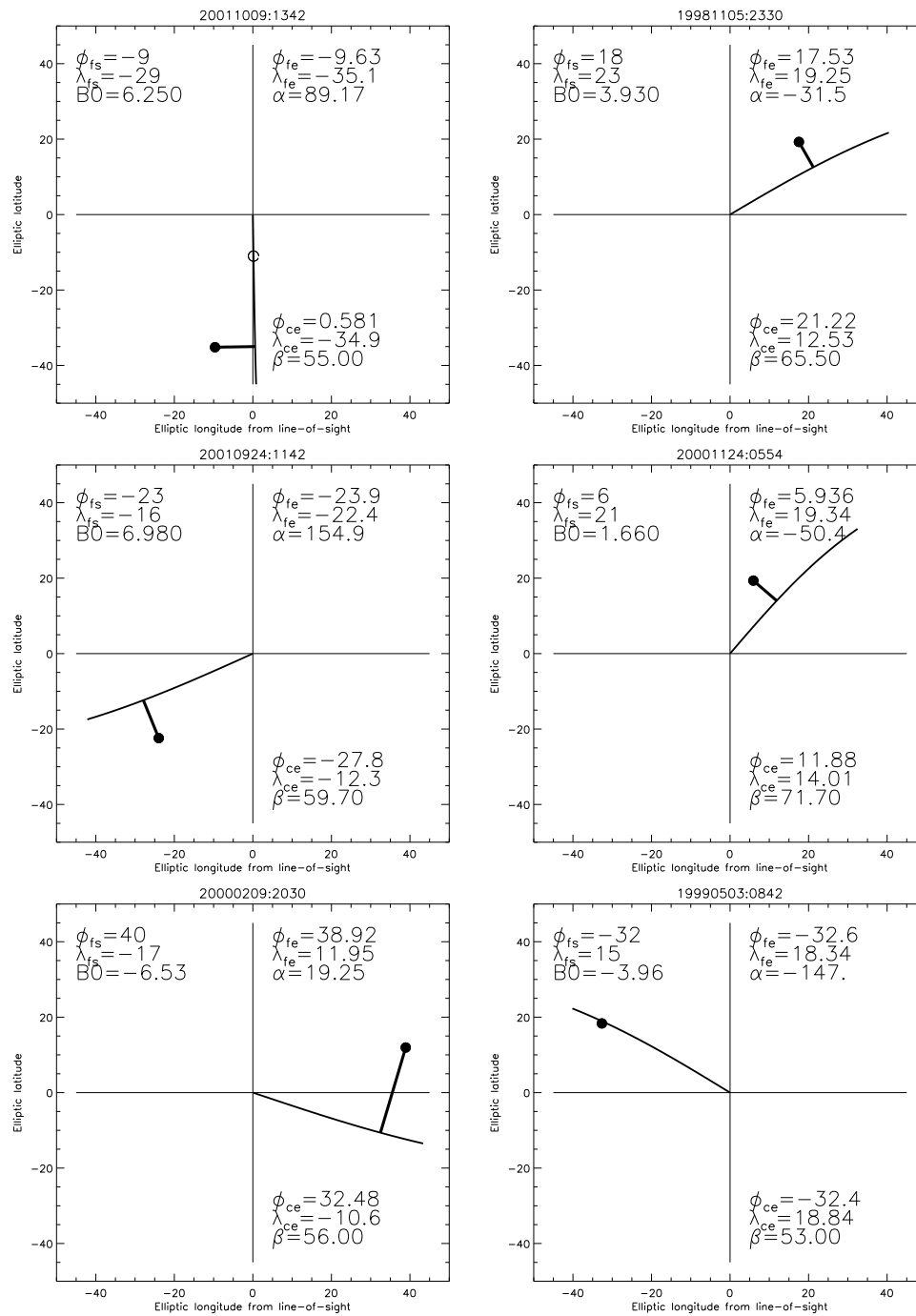


Figure 5. Description of the one-point approach for finding out the CME propagation direction (ϕ_{ce}, λ_{ce}) or β on the basis of halo parameter α and the location of CME-associated flare (ϕ_{fs}, λ_{se}). See text for details.

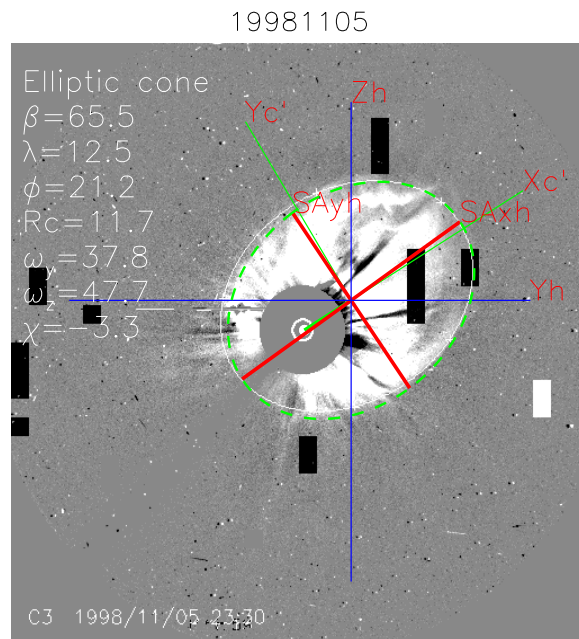
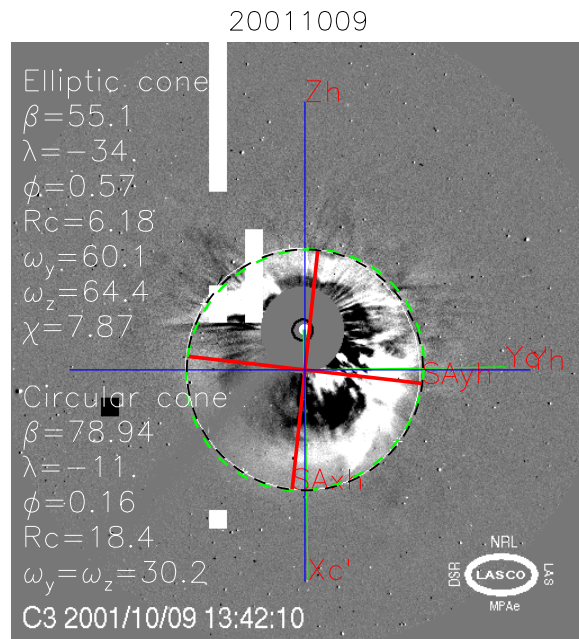


Figure 6. Elliptic and circular cone model parameters inverted using the halo parameters for the two halo events listed in the two top panels of Figure 1 and the parameter β inferred in the two top panels of Figure 4. The green and black dashed ellipses are calculated using the inverted elliptic and circular cone model parameters, respectively.

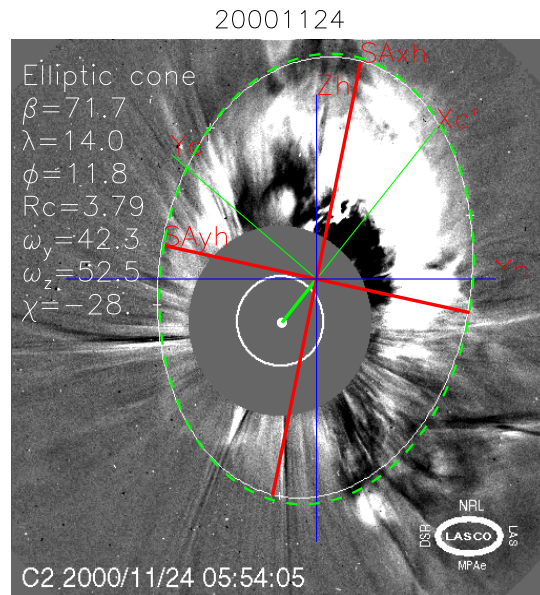
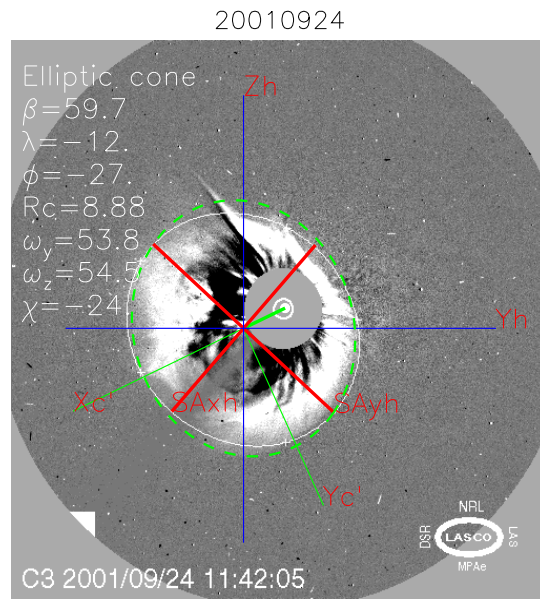


Figure 7. Elliptic cone model parameters inverted using the halo parameters for the two halo events listed in the two middle panels of Figure 1 and the parameter β inferred in the two middle panels of Figure 4. The green dashed ellipses are calculated using the inverted elliptic cone model parameters

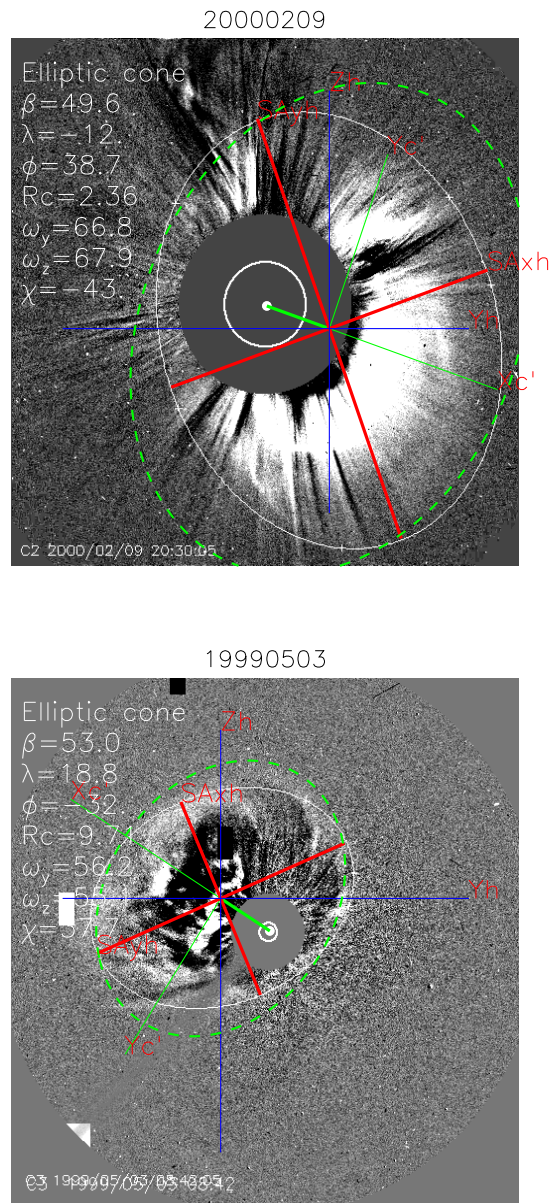


Figure 8. The same as Figure 7, but corresponding to the two halo events listed in the two bottom panels of Figure 1.